Journal of Materials Chemistry A

PAPER

View Article Online
View Journal | View Issue

Cite this: J. Mater. Chem. A, 2014, 2, 2306

Atomic layer deposited coatings to significantly stabilize anodes for Li ion batteries: effects of coating thickness and the size of anode particles†

Dongniu Wang,[ab] Jinli Yang,[a] Jian Liu,[a] Xifei Li,[a] Ruying Li,[a] Mei Cai,[c] Tsun-Kong Sham*[b] and Xueliang Sun*[a]

Received 13th September 2013
Accepted 17th November 2013

DOI: 10.1039/c3ta13677a

www.rsc.org/MaterialsA

A study of the effect of thickness of alumina coating on the electrochemical performances of various sizes of SnO_2 electrodes has been systematically studied in this paper. It is found that the different volume changes in various sizes of SnO_2 electrodes can be suppressed by optimized thickness of Al_2O_3 coating layers, with a range from less than 1 nm to up to 3 nm deposited by atomic layer deposition (ALD), which have significant impact on the electrochemical behaviour of the composites. The well-defined and optimized Al_2O_3 layer could not only relieve mechanical degradation and improve cycling stability, but also form an artificial solid electrolyte interphase (SEI) layer to prevent the chemical reaction between SnO_2 and the electrolyte, leading to improved electrochemical performances compared with bare SnO_2 electrodes.

Introduction

With the demand for alternative energy sources to replace conventional fossil fuels, lithium ion batteries (LIB) have been widely studied in recent years and are regarded as some of the most promising candidates.[1,2] More and more interest in LIB is focused on enhancing the lithium storage capability to satisfy the requirements of large-scale applications, such as electrical grids, hybrid electrical vehicles and full electrical vehicles.[3,4] The state-of-the-art LIB has limitations including safety concerns, high cost and low energy density. Such issues could be overcome by exploiting new types of electrode materials and attempting various electrode composites.[5–8]

Much research has concentrated on Sn-based anodes, originating from its attractive features including large reserves, environmental friendliness, low operating potential level and high lithium storage capability, which is more than twice of that of commercial graphite (*e.g.* 784 mA h g^{-1} for SnO_2, 992 mA h g^{-1} for Sn).[7,9] However, starting from the work of Idota,[10] more than a decade of research effort has been devoted to improving the cycling stability that remains hampered by volume variation (>300%) and the accompanying serious pulverization of electrodes, the undesired accumulation of a thick solid electrolyte interphase (SEI) layer, and the falling off of Sn-based materials. Among the approaches used to overcome these challenges, designing nanostructured Sn-based composites is regarded as one of the most effective strategies. Various Sn-based nanostructures and related composites, including tubular SnO_2/C nanoplates,[11] SnO_2 nanosheets,[12,13] hollow SnO_2[14] and $CoSn_3$/C nanostructures,[15] SnO_2 nanowire/C arrays,[16] SnO_2/graphene,[7,17] Sn/graphene,[18,19] SnO_2/Co_3O_4/C,[20] and SnO_2/SiC/graphene nanocomposites,[21] have been proposed and improved long life cycling and rate performances have been obtained. However, nanostructured electrodes possess a large amount of irreversible SEI due to the large contact area with electrolyte, resulting in low initial coulombic efficiency. Also, the mechanical and chemical degradation of the SEI will cause a vicious cycle, resulting in the depletion of the electrolyte and the waste of electrodes.

Surface modification of electrodes, especially surface coating on active materials, has been proved as an effective route to stabilize the SEI layer. Moreover, it could maintain the mechanical integrity of the whole electrode. A desired coating layer should be ionically conductive to facilitate charge transfer, while being mechanically and electrochemically stable to continuously prohibit the direct contact between electrolyte and electrodes. Meanwhile, the coating layer should be controlled in a limited amount to maximize the whole capacity of the composites. Recently, atomic layer deposition (ALD) has attracted great interest as a novel technique and a suitable

[a]Department of Mechanical and Materials Engineering, University of Western Ontario, London, Ontario, N6A 5B9, Canada. E-mail: xsun@eng.uwo.ca; Tel: +1 15196612111 ext. 87759

[b]Department of Chemistry, University of Western Ontario, London, Ontario, N6A 5B7, Canada. E-mail: tsham@uwo.ca; Tel: +1 15196612111 ext. 86341

[c]General Motors R&D Center, Warren, 48090-9055, MI, USA

† Electronic supplementary information (ESI) available: EDX spectrum of 20-SnO_2-C, SEM images of three sizes of SnO_2, TEM images of 20-SnO_2-A, 20-SnO_2-B, elemental mapping spectra of 20-SnO_2-A, charge–discharge profiles, cyclic voltammetry of electrodes, coulombic efficiency of SnO_2, EIS plots, ALD coated SnO_2 and elemental mapping spectra of 20-SnO_2-C after cycling. See DOI: 10.1039/c3ta13677a

approach for application in LIB because of its excellent capability to realize conformal coating of thin films in the scale of atomic layers.[22] The interest for LIB applications in our group is using ALD to synthesize various coatings[23] on cathodes and anodes, synthesize anode materials[24,25] and solid-state electrolytes. Work from other groups has also demonstrated that enhanced electrochemical performance was achieved using ALD coatings of metal oxides for cathodes, such as $LiCoO_2$,[26–29] $LiNi_{1/3}Mn_{1/3}Co_{1/3}O_2$[30–32] and $LiMn_2O_4$.[33,34] Dillon and coworkers demonstrated the success of MoO_3 electrodes with an Al_2O_3 coating.[35] Xiao[36] *et al.* and Huang[37] *et al.* reported the multifunctional effect of Al_2O_3 on Si thin film and patterned Si electrodes with improved current efficiency. Jung *et al.* found that a whole battery (separator, cathode and anode) with Al_2O_3 coating could endure extremely severe conditions, such as high voltage over 4.5 V.[38] However, to the best of our knowledge, few studies have been focused on ALD coatings on promising SnO_2-based anodes. Herein, we report a systematic study of the effect of the thickness of Al_2O_3 coating on the electrochemical behaviours of SnO_2 electrodes. To set up a simple but detailed model, electrodes composed of SnO_2 with three different sizes were chosen as references and compared with the Al_2O_3 coated electrodes. It was found that a well-defined and optimized Al_2O_3 coating could mitigate the mechanical and chemical degradation of the SEI layer and the electrodes, leading to improved electrochemical behaviour compared with pure SnO_2 electrodes.

Experimental methods

Synthesis of SnO_2 nanoparticles

In a typical synthesis of SnO_2 nanoparticles, 2 mmol $SnCl_4$ was dissolved in 10 mL water and vigorously stirred for 30 min to obtain a clear solution. Then the transparent solution was transferred to a 20 mL high pressure microwave-assisted Teflon-lined autoclave (Anton Paar Synthos 3000). The solution was subsequently heated to 120 °C and kept at this temperature for 20 min. After cooling to room temperature, the obtained samples were rinsed with large amounts of distilled water and ethanol. The as-obtained products were collected after a final drying at 100 °C overnight for use in the next step. To get three different sizes of SnO_2 nanoparticles, the products were annealed in a tube furnace at different temperatures for 2 h (400 °C for SnO_2-A, 600 °C for SnO_2-B and 900 °C for SnO_2-C, respectively).

Synthesis of ALD-Al_2O_3 coated SnO_2 electrodes

The working electrodes were composed of the SnO_2 nanomaterials (SnO_2-A, SnO_2-B or SnO_2-C), conductive carbon black and polyvinylidene fluoride (PVDF) in a weight ratio of 8 : 1 : 1. The slurry obtained with *N*-methylpyrrolidinone (NMP) solvent was uniformly cast on a copper foil and dried overnight at 70 °C under vacuum. The as-prepared electrodes were ready for ALD coating without further treatment. ALD-Al_2O_3 was coated directly on the SnO_2 electrodes in an ALD reactor (Savannah 100, Cambridge Nanotechnology Inc., USA) using trimethylaluminum (TMA) as the Al precursor and H_2O as the oxidizer. The deposition temperature was set at 100 °C. Different numbers of ALD cycles (2, 5 and 20 cycles) were used to get different thicknesses of coating layer. The coated electrodes were applied for LIB testing without further treatment.

Characterization

Products were characterized by X-ray diffraction (XRD, Rigaku RU-200BVH with a Co Kα source ($\lambda = 1.7892$ Å)), field-emission scanning electron microscopy (FE-SEM, Hitachi 4800S), transmission electron microscopy (TEM, Hitachi H-7000), high-resolution transmission electron microscopy (HRTEM, JEOL 2010 FEG microscope), and energy dispersive spectroscopy (EDX). X-ray absorption near edge structure (XANES) experiments on the Al K edge and the Al $L_{3,2}$ edge were conducted on the undulator Spherical Grating Monochromator (SGM) beamline and the variable line spacing plane grating monochromator (VLS PGM) beamline at the Canadian Light Source (CLS), located at the University of Saskatchewan in Saskatoon. Sn K edge XANES and extended X-ray absorption fine structure (EXAFS) data were obtained at the X-ray Science Division (XSD)/Pacific Northwest Consortium (PNC) at Sector 20 of the Advanced Photon Source located in the Argonne National Laboratory, and were recorded in fluorescence mode.

Electrochemical measurements

The electrochemical experiments were conducted using two electrode coin cells (2032) using pure lithium metal sheets as the counter electrode and polypropylene film as the separator assembled inside an argon-filled glove box (O_2 < 1 ppm). The electrolyte was 1.0 M $LiPF_6$ in a mixture of ethylene carbonate (EC) and dimethyl carbonate (DMC) solvent (1 : 1 in volume). The profiles of galvanostatic charging and discharging curves were collected on a computer controlled Arbin BT-2000 battery tester system with a cut-off voltage window of 0.01 to 3 V (*vs.* Li^+/Li). Cyclic voltammetry (CV) measurements were conducted on an electrochemical workstation (Potentiostat/Galvanostat/EIS (VMP3)) at a scanning rate of 0.1 mV s^{-1} in a voltage range of 0.01–3.0 V (*vs.* Li^+/Li). Electrochemical impedance spectroscopy (EIS) measurements were conducted by applying an AC voltage of 5 mV amplitude in the frequency range from 0.01 to 100 kHz at 0.7 V of the 10th discharge cycle.

Results and discussion

The SnO_2 nanoparticles were synthesized by a microwave-assisted hydrothermal method through the hydrolysis of $SnCl_4$ in aqueous solution at 120 °C for 20 min, followed by annealing at a selected temperature in air for 2 h. For distinction, the samples are denoted as SnO_2-A (annealed at 400 °C), SnO_2-B (annealed at 600 °C) and SnO_2-C (annealed at 900 °C). Then, an ALD coating of Al_2O_3 was directly applied on the electrodes composed of the SnO_2 nanomaterials. Al_2O_3 layers with different thicknesses were obtained by alternate pulses of $Al(CH_3)_3$ and water with 2, 5 and 20 ALD cycles at 100 °C, in a Savannah 100 ALD system. The Al_2O_3-coated SnO_2 electrodes

thus obtained were used without further treatment and are henceforth denoted as x-SnO_2-A, x-SnO_2-B and x-SnO_2-C (x = 2, 5, 20 for 2, 5 and 20 ALD cycles, respectively).

Fig. 1a compares the XRD patterns of different sized SnO_2 with and without Al_2O_3 coating, in which all the intense peaks match well with those of rutile SnO_2 (JCPDS no: 41-1445), indicating that crystallized SnO_2 is successfully synthesized without detectable impurities. Further closer examination shows that the XRD pattern of SnO_2-C is stronger and sharper than those of SnO_2-B and SnO_2-A, illustrating the higher crystallinity of SnO_2-C due to the higher temperature annealing. Also, the XRD peaks for SnO_2-C are narrower than those of SnO_2-B and SnO_2-A, indicating that the grain size in this sample is bigger. Based on calculation using Scherrer's equation from the strongest peak, average particle sizes of 4.1, 8.8 and 25.8 nm are obtained for SnO_2-A, SnO_2-B and SnO_2-C, respectively. It should be noted that no peaks for the Al_2O_3 phase were observed in any of the Al_2O_3-coated SnO_2 samples, which is due to its amorphous structure, considering that the ALD deposited Al_2O_3 was obtained at 100 °C. Fig. S1a† displays the energy dispersive X-ray (EDX) spectrum of 20-SnO_2-C. The appearance of the Al signal conclusively illustrates that Al element is successfully introduced into SnO_2 composites. To identify the chemical states of Al, X-ray absorption near edge structure (XANES) was conducted at the Al K edge for the 20-SnO_2-C electrode. As depicted in Fig. 1b, the Al K edge spectrum of the 20-SnO_2-C electrode is similar to that of standard α-Al_2O_3, indicating the formation of Al_2O_3 after the ALD process. Compared with standard Al_2O_3, which exhibits two resolved peaks centered at 1567 and 1571 eV, the spectrum of 20-SnO_2-C shows fewer features, with only one broad peak located at 1570 eV, confirming its amorphous state. The XANES results demonstrate that amorphous Al_2O_3 was successfully coated on the SnO_2 anodes.

The morphologies of SnO_2 and the Al_2O_3 coating layer were examined using TEM, as shown in Fig. 2. Three different sizes of SnO_2 nanoparticles with average diameters of 3 nm, 10 nm and 25 nm are unambiguously shown in Fig. 2a–c, respectively. Fig. S1b to S1d† depict the SEM images of the different sized SnO_2, where spherical nanoparticles exhibit a uniform size distribution. Higher temperature annealing will facilitate the growth rate of crystallites, leading to a bigger particle size. Meanwhile, all particles show high crystallinity with clean surfaces, as demonstrated by the clear lattice fringes of the HRTEM images. The morphologies of the 2-SnO_2-C, 5-SnO_2-C and 20-SnO_2-C composites are shown in Fig. 2d–f. For 2-SnO_2-C, the Al_2O_3 coating layer is hard to observe because of the thickness (too thin), as it was formed by only 2 ALD cycles. After 5 cycles, it is evident that a conformal Al_2O_3 layer is successfully coated on the surface of the SnO_2 particles, which presents a distinct contrast under electron spectroscopy compared to that of the crystallized SnO_2. With the increase of the number of ALD cycles from 5 to 20, the thickness of the Al_2O_3 layer increased from ~0.8 nm to ~3.1 nm, illustrating that the thickness of Al_2O_3 could be precisely tuned by the number of ALD cycles. The Al_2O_3 shell displays no crystalline features in either sample, which is consistent with the XANES result. A uniform Al_2O_3 coating layer with similar thickness could also be found for 20-SnO_2-A and 20-SnO_2-B electrodes, as revealed in Fig. S2.† EDX mapping (Fig. S3†) of 20-SnO_2-A further confirms the homogeneous distribution of Al element, while the carbon signal comes from the conductive carbon black applied for preparation of the electrodes. Al_2O_3 could be homogeneously deposited on different sized SnO_2 electrodes using the ALD technique, which is critical for optimal electrochemical behaviour.

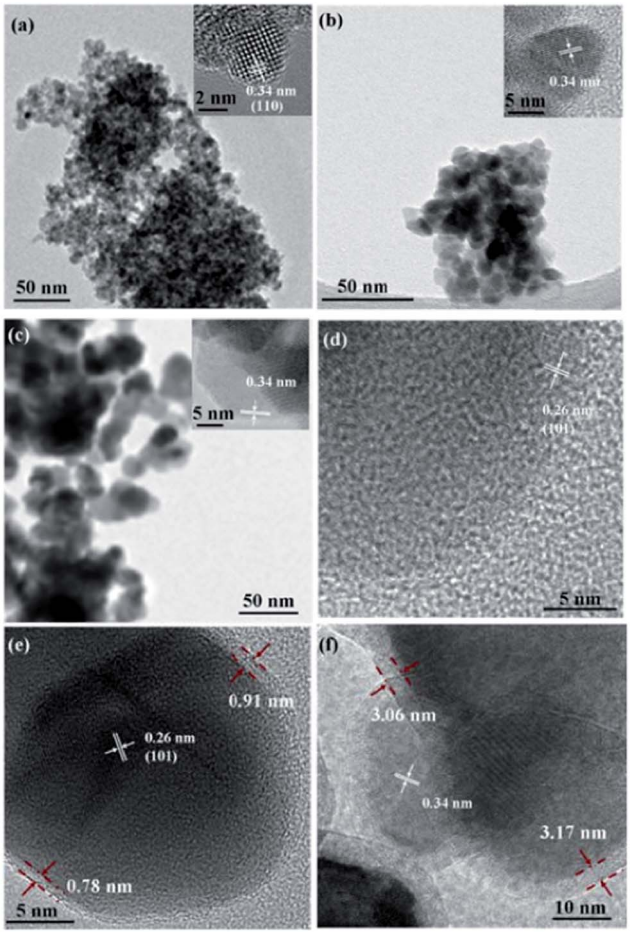

Fig. 2 TEM images of SnO_2 (insets show HRTEM images of single particles) and Al_2O_3-coated SnO_2 samples: (a) SnO_2-A; (b) SnO_2-B; (c) SnO_2-C; (d) 2-SnO_2-C; (e) 5-SnO_2-C; (f) 20-SnO_2-C.

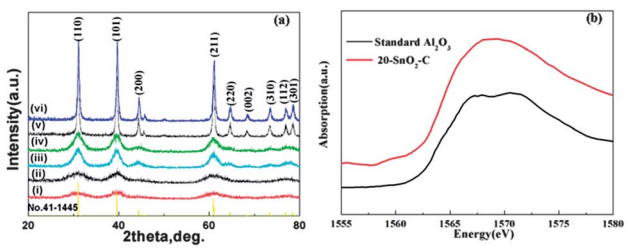

Fig. 1 (a) XRD patterns of different sizes of SnO_2: (i) SnO_2-A; (ii) 20-SnO_2-A; (iii) SnO_2-B; (iv) 20-SnO_2-B; (v) SnO_2-C; (vi) 20-SnO_2-C; (b) Al K edge XANES of 20-SnO_2-C and standard Al_2O_3.

The electrochemical performances of the obtained Al_2O_3-coated electrodes and their uncoated counterparts are compared in Fig. 3. Cyclic performances were measured in a voltage window from 0.01 to 3 V with a current density of 50 mA g^{-1}. The rate performances were recorded at various current densities of 50 up to 1000 mA g^{-1}, and then reversed back to 50 mA g^{-1}. As presented in Fig. 3a and b, SnO_2-A delivers an initial discharge capacity of 1951 mA h g^{-1} and stabilizes from the 20th cycle, retaining 530 mA h g^{-1} in the 60th cycle. It should be noted that since the particle size of SnO_2-A is small enough (3 nm) and below the critical size,[39] the stress and strain caused by volume change is not serious and thus stable discharge and charge capacities were obtained. For the Al_2O_3-coated samples with various numbers of ALD coating cycles, all samples still exhibit stable cycling performance, but their specific capacities are obviously different. The 2-SnO_2-A and 5-SnO_2-A samples exhibit increased capacities of 883 mA h g^{-1} and 612 mA h g^{-1} in the 60th cycle, respectively, while the 20-cycle-coated sample maintains a decreased capacity of 420 mA h g^{-1}. Noting that the Al_2O_3 layer is thin but conformally coated on SnO_2 in 2-SnO_2-A and 5-SnO_2-A, the coated Al_2O_3 could effectively inhibit the direct contact between SnO_2 and the electrolyte, reducing the amount of SEI which is unstable and easily degraded mechanically, and avoiding the consumption of active materials thus leading to increased capacities. For 20-SnO_2-A, the coating thickness is comparable to the size of the SnO_2 particles, as depicted in Fig. S2a.† Since bare electrodes already display a steady cycling performance, a thicker Al_2O_3 coating layer could only result in a lower capacity in view of the whole electrode. The 2-cycle ALD coating is demonstrated as the optimal coating layer for SnO_2-A. A comparison of the first two charge–discharge profiles of bare SnO_2-A and 2-SnO_2-A shows similar plateaus of the two electrodes, indicating that the Al_2O_3 layer has little effect on the potential plateaus of SnO_2, as presented in Fig. S4.† The initial plateau located between 1.2 V and 0.8 V is due to the conversion reaction between SnO_2 and Li^+ and the formation of Sn and Li_2O.[7] The following long slope profile is due to the formation of Li–Sn alloys. Bare SnO_2-B exhibits poorer cyclic performance compared with SnO_2-A due to the larger particle size and the accompanying large expansion/contraction of volume, as illustrated in Fig. 3c. In the 60th cycle, the capacity drops to only 220 mA h g^{-1}.

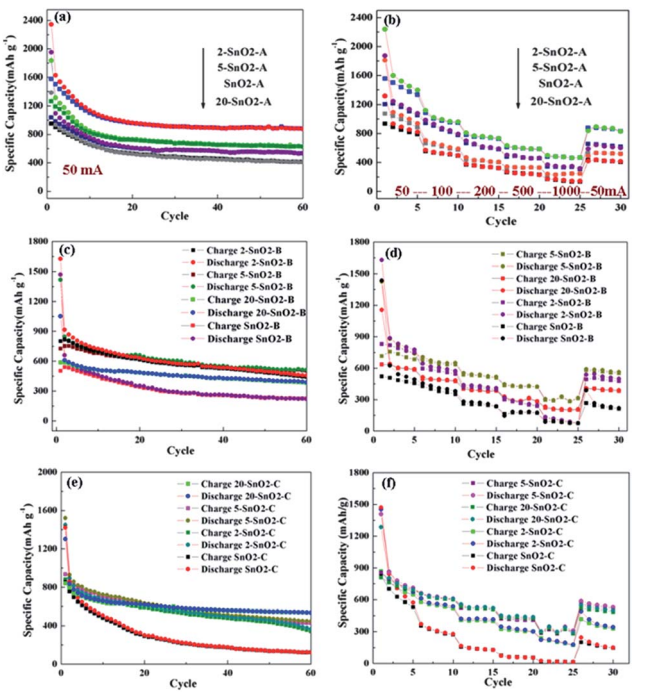

Fig. 3 (a, c, and e) Cycling performances (at 50 mA g^{-1}) and (b, d, and f) rate performances (at 50 mA g^{-1} to 1000 mA g^{-1}) of Al_2O_3-coated and non-coated SnO_2 samples: (a and b) SnO_2-A series; (c and d) SnO_2-B series; (e and f) SnO_2-C series.

For the ALD-coated SnO_2-B electrodes, they all exhibit improved lithium storage capabilities. As depicted in Fig. 3d, in the 60th cycle, 2-SnO_2-B, 5-SnO_2-B and 20-SnO_2-B show capacities of 456, 512 and 388 mA h g^{-1}, respectively. The cycling stabilities follow the order: 20-SnO_2-B > 5-SnO_2-B > 2-SnO_2-B. For 2-SnO_2-B, there was only a 2-cycle ALD coating layer (less than 0.2 nm empirically) and the coating could not radically buffer the volume change of SnO_2-B during cycling very well. Thus 2-SnO_2-B shows poorer cycling performance than 5-SnO_2-B and 20-SnO_2-B. Similar phenomena could also be observed for the rate performances of different ALD coated electrodes, where the 2-SnO_2-B sample also exhibits fast decay of performance at high rates. In contrast, for the 5-SnO_2-B and 20-SnO_2-B composites, the coating layer could not only prevent the formation of a large amount of SEI, but more importantly, it can effectively absorb the strain and stress, providing a cushioning effect. For the 10 nm sized SnO_2-B, the 5 cycle ALD coating is found to be the optimal coating. For the biggest sized SnO_2-C shown in Fig. 3e, the SnO_2-C electrode shows the poorest cycling performance among all three bare electrodes, retaining a capacity of only 123 mA h g^{-1} in the 60th cycle due to its large volume variation. For the coated samples shown in Fig. 3f, it is clear that the Al_2O_3 coating can significantly improve the stabilities for all three specified ALD cycles. For SnO_2-C, it is demonstrated that the 20-SnO_2-C sample exhibits the best cycling stability, presenting a capacity of 535 mA h g^{-1} in the 60th cycle, which is four times higher than that of pure SnO_2-C. For 5-SnO_2-C and 2-SnO_2-C, the tendency for capacity decrease is inevitable, resulting in capacities of 446 and 365 mA h g^{-1}, respectively in the 60th cycle. The poorer cycling capabilities of these samples compared with that of 20-SnO_2-C indicate that the coating layer from 2 or 5 cycles of ALD is not robust enough to endure the expansion/contraction of SnO_2-C during prolonged cycling. Similarly, the rate performance profiles further confirmed the increased stabilities for ALD-coated samples due to the protection from the outer Al_2O_3 layer. Fig. S5† presents the first three CV curves of SnO_2-C and 20-SnO_2-C. The shape of the CV curves for the coated electrodes is quite similar to that for the pure SnO_2-C electrode, indicating that the coating layer has no effect on the reaction mechanism of SnO_2 with lithium. The reduction peak at 0.78 V can be attributed to Li insertion into SnO_2, accompanied by the phase transformation of SnO_2 to Sn and Li_2O.[7,33] The second pronounced reduction peak at

around 0.25 V can be ascribed to the alloying of lithium with Sn to form Li_xSn.

For the anodic scan, the peaks located at ~0.52 V correspond to the dealloying of Li_xSn. It can be seen that for the 20-SnO_2-C sample, the oxidation peaks at 0.53 V decreased less than those of the pure SnO_2-C electrode, indicating the improved stability due to the coating layer. Xiao[36] *et al.* also reported that Al_2O_3 could react with lithium ions and the electrolyte to form an artificial solid electrolyte interphase layer, thus improving the ionic conductivity, which is favourable for high rate performance and enhanced current efficiency. As shown in Fig. S6,† compared with the uncoated SnO_2 samples, all Al_2O_3-coated SnO_2 samples exhibit improved current efficiency, especially in the first ten cycles, benefiting from the Al_2O_3 layer which forms an artificial ionically conductive SEI layer and prevents the mechanical and electrochemical degradation of the electrodes. The thickest coating exhibits the best coulombic efficiency due to its more robust framework and highly ionic conductive channels. Fig. S7† exhibits the electrochemical impedance spectroscopy for pure SnO_2-C and 20-SnO_2-C electrodes, conducted at 0.7 V in the 10th discharge cycle. It is evident that the diameter of the semicircle for 20-SnO_2-C is much smaller compared with that of pure SnO_2 upon cycling, indicating the lower impedance value due to the ALD-alumina coating. The enhanced ionic conductivity in the composites should be attributed to the artificial ionically conductive SEI layer mentioned above, which facilitates Li^+ alloying and dealloying into the anodes.

In order to examine the morphology evolution of the SnO_2 particles after cycling, HRTEM was performed, as shown in Fig. 4. For the pure SnO_2-A electrode shown in Fig. 4a, patches of blurry SEI film can be observed, as indicated by the arrows. Some crystallites can also be found, however, the size of the particles became irregular due to pulverization and they tend to aggregate to form bigger particles (as indicated by the circles). It is believed that the pulverization of SnO_2 will produce new fresh surface, which leads upon contact with the electrolyte to the formation of more and more SEI (marked by arrows) and consumption of the active materials. Conversely, after cycling, the 2-SnO_2-A electrode still maintains its original morphology without obvious change of particle size, as depicted in Fig. 4b. A careful examination illustrates that a thin layer appeared on the outside of the nanoparticles (as depicted by the dotted lines), which is absent in the original 2-SnO_2-A particles before cycling. The thin layer seen here should be ascribed to the artificial SEI layer formed by the reaction of Al_2O_3 with the electrolyte or lithium ions.[36] This artificial SEI layer is ionically conductive and could mitigate the pulverization of the SnO_2 core, inhibit the formation of undesired SEI between SnO_2 and the electrolyte and result in excellent electrochemical behavior. Similar to that reported recently by Hu *et al.*,[40] improved cycling behavior and safety are also realized through the reduction of SEI thickness by using high concentration electrolyte. For the bare SnO_2-C electrode after cycling, the SnO_2 particles were pulverized into small particles without crystalline features, as shown in Fig. 4c. Also, a thick SEI film of around 6.8 nm accumulated at the surface of small particles (as indicated by the arrow)

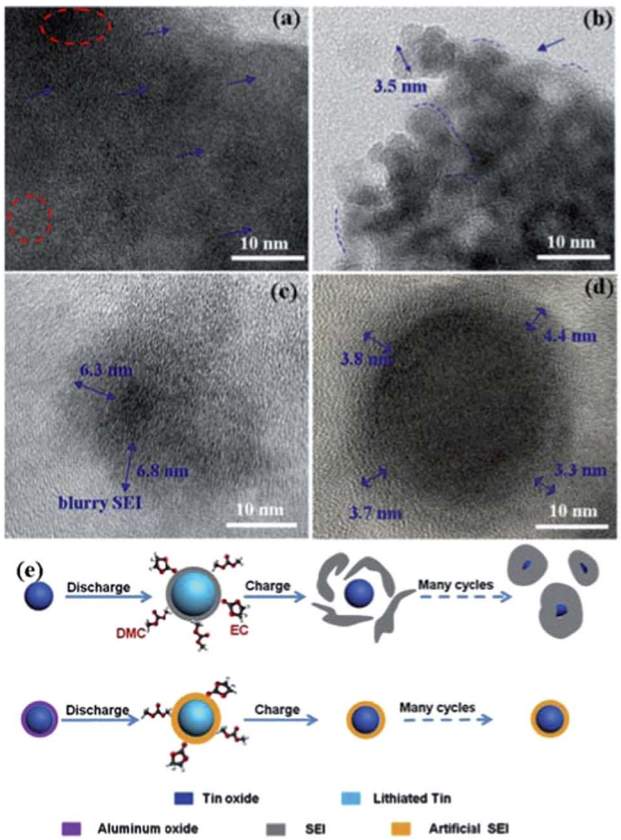

Fig. 4 TEM images of (a) SnO_2-A and (b) 2-SnO_2-A after 60 cycles at 50 mA g^{-1}. (c) SnO_2-C and (d) 20-SnO_2-C after 60 cycles at 50 mA g^{-1}. (e) Schematic representation showing SEI formation on pure SnO_2 and Al_2O_3-coated SnO_2 upon cycling.

through the reaction of the electrolyte with the continuously emerging fresh surface of SnO_2-C due to the pulverization. The unstable and non-uniformly covered SEI film could deteriorate the cycling performances of the electrodes. In contrast, for the cycled 20-SnO_2-C electrodes shown in Fig. 4d, the spherical particles are still well maintained under the protection of the outer shell which expands a little compared with that before cycling. The swollen shell may be due to the reaction of lithium ions or electrolyte with Al_2O_3 to form an ionically conductive SEI layer with an average thickness of around 3.8 nm. More importantly, the SnO_2 core without pulverization showed that the highly stable artificial SEI layer could effectively buffer the stress and strain upon cycling. Elemental mapping was further performed on the 20-SnO_2-C electrode after 60 cycles, as shown in Fig. S8.† The distribution of Al is still homogeneous in the electrode after cycling, along with the F signal, illustrating that the artificial SEI is tightly attached to the inside core and the integrity of the electrode is well maintained. Fig. 4e shows the schematic representation of ALD-coated and bare SnO_2 electrodes during cycling, where the coating layer could form an artificial SEI layer to effectively inhibit the detrimental reaction between SnO_2 and the electrolyte. As a result, improved cycling performance and rate performances were obtained for the optimal ALD-coated SnO_2 electrodes.

To reveal the local chemistry environment variation of the SnO_2 electrodes behind their different electrochemical performances, Sn K edge XANES was performed on the 2 cycle ALD-coated and non-coated SnO_2-A electrodes before and after cycling. As shown in Fig. 5, it can be seen that the spectrum of 2-SnO_2-A overlapped well with that of pure SnO_2-A, illustrating that the deposition of Al_2O_3 did not affect the local symmetry and chemical states of SnO_2. After 60 cycles, the spectrum of the SnO_2-A electrodes became broader with a slight shift of the white line towards lower energy, indicating a more disordered structure with reduced valence states. More intriguingly, for 2-SnO_2-A after cycling, the line shape is identical to that of the 2-SnO_2-A, illustrating that the outer Al_2O_3 shell could effectively protect the integrity and crystallinity of the core SnO_2. Fig. 5b shows the Fourier transform magnitudes of the Sn K edge Extended X-ray Absorption Fine Structure (EXAFS) spectra. All four samples exhibit similar spectral features except for the different magnitudes, illustrating the different average coordination numbers of Sn and hence the disorder among them. It is found that the magnitude of the Sn–O nearest neighbour distance decreases a little after coating with Al_2O_3, indicating that the outer Al_2O_3 shell may affect the ordered arrangement of the SnO_2 particles. For bare SnO_2-A after cycling, the magnitudes decreased considerably, demonstrating an increase of the disorder inside the crystallite and a decrease of the crystallite size, which is in accordance with the HRTEM results. However, for 2-SnO_2-A after cycling, the decrease of magnitude is not significant, indicating that both the crystallinity and the size of the crystallites are well maintained by the coating layer.

We further conducted Al $L_{3,2}$ edge XANES experiments on the 20-SnO_2-C electrodes before and after cycling to reveal the electronic structure variation. XANES spectra of two major components, the $LiAlO_2$ and AlF_3 in the artificial SEI layer as reported by Xiao *et al.*,[36] are also given for comparison, as shown in Fig. 6. It can be clearly seen that after cycling, the Al L edge XANES for 20-SnO_2-C is quite different compared with that before cycling, as seen in the peak positions and intensities. The two features located at c and d correspond to the amorphous Al_2O_3, which is in accordance with our previous results, indicating a six-fold coordination.[42,43] After cycling, the spectra became broader, with peak a shifted to lower energy, indicating a phase transition induced by the lithium and fluoride ions. Closer observation demonstrates that it shows similar features

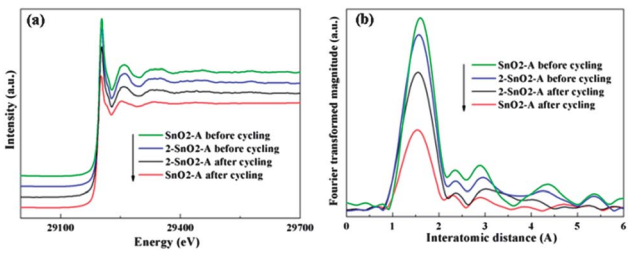

Fig. 5 (a) XANES of Sn K edge spectrum and (b) Fourier-transformed[41] magnitudes of Sn K edge k^3-weighted EXAFS spectra for 2 cycle ALD-coated and bare SnO_2 electrodes, before and after cycling.

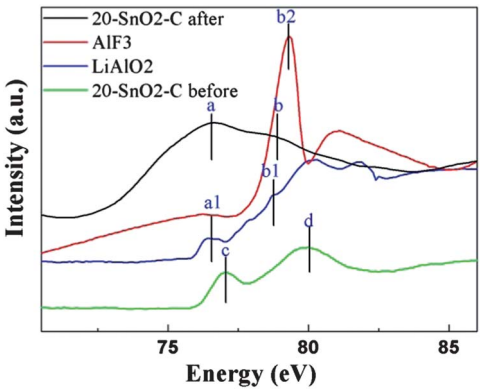

Fig. 6 Al $L_{3,2}$-edge XANES of AlF_3, $LiAlO_2$ and the 20-SnO_2-C electrode before and after cycling.

to that of $LiAlO_2$ in the first peak (a and a1) and mixed features of $LiAlO_2$ and AlF_3 in the following shoulder (b, b1, and b2). It should be noted that the Al L-edge spectrum (2p electrons to 3d or 3s) is sensitive to Al coordination number and the surrounding atoms. Also, the artificial SEI layer presented here is amorphous and quite thin (only a few nanometers), which leads to a broader and more irregular spectrum. Thus, XANES spectra provide spectroscopic evidence that an artificial SEI layer is formed after the lithiation/delithiation process, with a major composition of ionic conductive $LiAlO_2$ and AlF_3. The ALD-Al_2O_3 coating layer helps to maintain the size and structure of the SnO_2 electrodes and facilitates charge transfer at the interface, resulting in more stable electrochemical behaviour compared with the pristine electrodes.

Conclusions

In summary, a controlled Al_2O_3 layer has been successfully coated on different sizes of SnO_2 particles using the ALD technique. As demonstrated by the HRTEM results and the synchrotron radiation spectra, well-defined and optimized Al_2O_3 coating layers could maintain the integrity of the electrodes by suppressing the volume change to improve the cycling performances. It could also function as an artificial ionic conductive SEI layer and inhibit direct contact between SnO_2 and the electrolyte to increase the rate capability and the coulombic efficiency. This work opens up a path for studying the connection between the coating layer and the inner active electrodes, and will inspire future applications of the ALD technique in electrodes for lithium ion batteries.

Notes and references

1 A. K. Padhi, K. S. Nanjundaswamy and J. B. Goodenough, *J. Electrochem. Soc.*, 1997, **144**, 1188–1194.
2 L. X. Yuan, Z. H. Wang, W. X. Zhang, X. L. Hu, J. T. Chen, Y. H. Huang and J. B. Goodenough, *Energy Environ. Sci.*, 2011, **4**, 269–284.
3 L. F. Shen, E. Uchaker, X. G. Zhang and G. Z. Cao, *Adv. Mater.*, 2012, **24**, 6502–6506.

4 L. Wang, X. M. He, W. T. Sun, J. L. Wang, Y. D. Li and S. S. Fan, *Nano Lett.*, 2012, **12**, 5632–5636.
5 J. L. Yang, J. J. Wang, D. N. Wang, X. F. Li, D. S. Geng, G. X. Liang, M. Gauthier, R. Y. Li and X. L. Sun, *J. Power Sources*, 2012, **208**, 340–344.
6 M. Ben Yahia, F. Lemoigno, G. Rousse, F. Boucher, J. M. Tarascon and M. L. Doublet, *Energy Environ. Sci.*, 2012, **5**, 9584–9594.
7 D. N. Wang, X. F. Li, J. J. Wang, J. L. Yang, D. S. Geng, R. Y. Li, M. Cai, T. K. Sham and X. L. Sun, *J. Phys. Chem. C*, 2012, **116**, 22149–22156.
8 Z. Y. Wang, D. Y. Luan, S. Madhavi, Y. Hu and X. W. Lou, *Energy Environ. Sci.*, 2012, **5**, 5252–5256.
9 D. Wang, X. Li, J. Yang, J. Wang, D. Geng, R. Li, M. Cai, T. K. Sham and X. Sun, *Phys. Chem. Chem. Phys.*, 2013, **15**, 3535–3542.
10 Y. Idota, T. Kubota, A. Matsufuji, Y. Maekawa and T. Miyasaka, *Science*, 1997, **276**, 1395–1397.
11 L. Zhang, G. Q. Zhang, H. B. Wu, L. Yu and X. W. Lou, *Adv. Mater.*, 2013, **25**, 2589–2593.
12 J. S. Chen and X. W. Lou, *Mater. Today*, 2012, **15**, 246–254.
13 S. J. Ding and X. W. Lou, *Nanoscale*, 2011, **3**, 3586–3588.
14 Z. Y. Wang, Z. C. Wang, S. Madhavi and X. W. Lou, *Chem.–Eur. J.*, 2012, **18**, 7561–7567.
15 Z. Y. Wang, Z. C. Wang, W. T. Liu, W. Xiao and X. W. Lou, *Energy Environ. Sci.*, 2013, **6**, 87–91.
16 S. J. Ding, Z. Y. Wang, S. Madhavi and X. W. Lou, *J. Mater. Chem.*, 2011, **21**, 13860–13864.
17 S. M. Paek, E. Yoo and I. Honma, *Nano Lett.*, 2009, **9**, 72–75.
18 B. Luo, B. Wang, X. L. Li, Y. Y. Jia, M. H. Liang and L. J. Zhi, *Adv. Mater.*, 2012, **24**, 5525.
19 L. W. Ji, Z. K. Tan, T. Kuykendall, E. J. An, Y. B. Fu, V. Battaglia and Y. G. Zhang, *Energy Environ. Sci.*, 2011, **4**, 3611–3616.
20 Y. Qi, H. Zhang, N. Du, C. X. Zhai and D. R. Yang, *RSC Adv.*, 2012, **2**, 9511–9516.
21 Z. X. Chen, M. Zhou, Y. L. Cao, X. P. Ai, H. X. Yang and J. Liu, *Adv. Energy Mater.*, 2012, **2**, 95–102.
22 X. B. Meng, X. Q. Yang and X. L. Sun, *Adv. Mater.*, 2012, **24**, 3589–3615.
23 J. Liu, X. B. Meng, M. N. Banis, M. Cai, R. Y. Li and X. L. Sun, *J. Phys. Chem. C*, 2012, **116**, 14656–14664.
24 X. B. Meng, J. Liu, X. F. Li, M. N. Banis, J. L. Yang, R. Y. Li and X. L. Sun, *RSC Adv.*, 2013, **3**, 7285–7288.
25 X. F. Li, X. B. Meng, J. Liu, D. S. Geng, Y. Zhang, M. N. Banis, Y. L. Li, J. L. Yang, R. Y. Li, X. L. Sun, M. Cai and M. W. Verbrugge, *Adv. Funct. Mater.*, 2012, **22**, 1647–1654.
26 J. T. Lee, F. M. Wang, C. S. Cheng, C. C. Li and C. H. Lin, *Electrochim. Acta*, 2010, **55**, 4002–4006.
27 I. D. Scott, Y. S. Jung, A. S. Cavanagh, Y. F. An, A. C. Dillon, S. M. George and S. H. Lee, *Nano Lett.*, 2011, **11**, 414–418.
28 H. M. Cheng, F. M. Wang, J. P. Chu, R. Santhanam, J. Rick and S. C. Lo, *J. Phys. Chem. C*, 2012, **116**, 7629–7637.
29 Y. S. Jung, P. Lu, A. S. Cavanagh, C. Ban, G. H. Kim, S. H. Lee, S. M. George, S. J. Harris and A. C. Dillon, *Adv. Energy Mater.*, 2013, **3**, 213–219.
30 Y. S. Jung, A. S. Cavanagh, Y. F. Yan, S. M. George and A. Manthiram, *J. Electrochem. Soc.*, 2011, **158**, A1298–A1302.
31 L. A. Riley, S. Van Ana, A. S. Cavanagh, Y. F. Yan, S. M. George, P. Liu, A. C. Dillon and S. H. Lee, *J. Power Sources*, 2011, **196**, 3317–3324.
32 M. Bettge, Y. Li, B. Sankaran, N. D. Rago, T. Spila, R. T. Haasch, I. Petrov and D. P. Abraham, *J. Power Sources*, 2013, **233**, 346–357.
33 D. S. Guan, J. A. Jeevarajan and Y. Wang, *Nanoscale*, 2011, **3**, 1465–1469.
34 X. Luan, D. Guan and Y. Wang, *J. Nanosci. Nanotechnol.*, 2012, **12**, 7113–7120.
35 L. A. Riley, A. S. Cavanagh, S. M. George, Y. S. Jung, Y. F. Yan, S. H. Lee and A. C. Dillon, *ChemPhysChem*, 2010, **11**, 2124–2130.
36 X. C. Xiao, P. Lu and D. Ahn, *Adv. Mater.*, 2011, **23**, 3911–3915.
37 Y. He, X. Q. Yu, Y. H. Wang, H. Li and X. J. Huang, *Adv. Mater.*, 2011, **23**, 4938–4941.
38 Y. S. Jung, A. S. Cavanagh, L. Gedvilas, N. E. Widjonarko, I. D. Scott, S. H. Lee, G. H. Kim, S. M. George and A. C. Dillon, *Adv. Energy Mater.*, 2012, **2**, 1022–1027.
39 C. Kim, M. Noh, M. Choi, J. Cho and B. Park, *Chem. Mater.*, 2005, **17**, 3297–3301.
40 L. Suo, Y. S. Hu, H. Li, M. Armand and L. Q. Chen, *Nat. Commun.*, 2013, **4**, 1481.
41 G. Croft and M. J. Fuller, *Nature*, 1977, **269**, 585–586.
42 Z. Wang, C. Li, L. Liu and T. K. Sham, *J. Chem. Phys.*, 2013, **138**, 084706.
43 Y. F. Hu, R. K. Xu, J. J. Dynes, R. I. R. Blyth, G. Yu, L. M. Kozak and P. M. Huang, *Geochim. Cosmochim. Acta*, 2008, **72**, 1959–1969.

